Pergamon

Planet. Space Sci., Vol. 45, No. 2, pp. 201–219, 1997

0032–0633/97 $17.00+0.00

PII: S0032–0633(96)00074–8

Lower hybrid waves generated in the wake of the Galileo spacecraft

A. E. Keller, D. A. Gurnett, W. S. Kurth, Y. Yuan and A. Bhattacharjee

Department of Physics and Astronomy, The University of Iowa, Iowa City, IA 52242, U.S.A.

Received 9 October 1995; revised 27 March 1996; accepted 30 April 1996

Abstract. During the first Earth flyby of the Galileo spacecraft, which occurred on December 8, 1990, spin modulated bursts of broadband electrostatic noise were observed with an intensification near the local lower hybrid frequency. These bursts occurred while the spacecraft was passing through the plasmasphere, where both the plasma density and the magnetic field strength are relatively high. By analyzing the spin modulation, which consisted of one burst per spacecraft rotation, it is shown that the waves are generated in the spacecraft wake. As a possible explanation for the observations, it is suggested that plasma density gradients in the wake could produce the waves via the electrostatic lower-hybrid-drift instability (LHDI). Numerical solutions of the dispersion relation show that strong wave growth occurs over a broad frequency range, with a peak growth rate near the lower hybrid resonance frequency. The numerical analysis also demonstrates that the LHDI occurs over a wide range of plasma parameters, including those that are believed to exist in the wake. These results also suggest that lower hybrid waves previously believed by other researchers to be of natural origin may in fact have been generated in spacecraft wakes via the LHDI or other wake-related mechanism.

1. Introduction

The Galileo spacecraft, which is on its way to Jupiter, made two flybys of Earth, the first on December 8, 1990, and the second on December 8, 1992. During the first Earth flyby, the plasma wave instrument detected an unusual type of broadband plasma wave emission with characteristics that have never been previously observed. The emission occurred relatively close to the Earth (<3 Earth radii (R_E)) and had a maximum intensity near the lower hybrid resonance frequency. The unique, new characteristic of this emission is that the electric field intensity was modulated at the spacecraft rotation rate, with one peak per rotation. This modulation pattern is not consistent with the wave field of any known naturally occurring magnetospheric emission. The Galileo plasma wave instrument is unusual in that the dipole electric antenna is mounted on the end of a long boom at a distance of 10.6 m from the center of the spacecraft body. Subsequent analyses show that the maximum electric field intensities occurred when the spacecraft was oriented such that the Earth's magnetic field connected the electric antenna to the downstream wake. Thus, it appears that the waves were generated in the spacecraft wake.

The purpose of this paper is to describe the wake-induced waves detected by Galileo and to propose a possible mechanism for their generation. We begin with a brief discussion of the spacecraft trajectory and a description of the plasma wave instrumentation (Section 2), followed by a description of the measurements (Section 3). In Section 4, the methods for determining the location of the source are discussed, including a simple wake model that helps refine the geometry of the emission region. In Section 5 we propose a theoretical mechanism for generating the waves, and in Section 6 we conclude with a summary and comments on some of the questions raised, including the possibility that waves previously detected by other spacecraft near the lower hybrid resonance frequency could be generated by some similar wake-induced instabilities.

2. Spacecraft trajectory and instrumentation

The primary period of interest in this paper is the first Galileo flyby of the Earth, which occurred on December 8, 1990. Although similar waves were detected during the second flyby, the emissions were weaker and more difficult to identify; thus, we have concentrated our analysis entirely on the first flyby. The spacecraft trajectory during the first flyby is shown in Fig. 1 using Geocentric Solar Magnetospheric (GSM) coordinates. The x-axis in this

Correspondence to: A. E. Keller

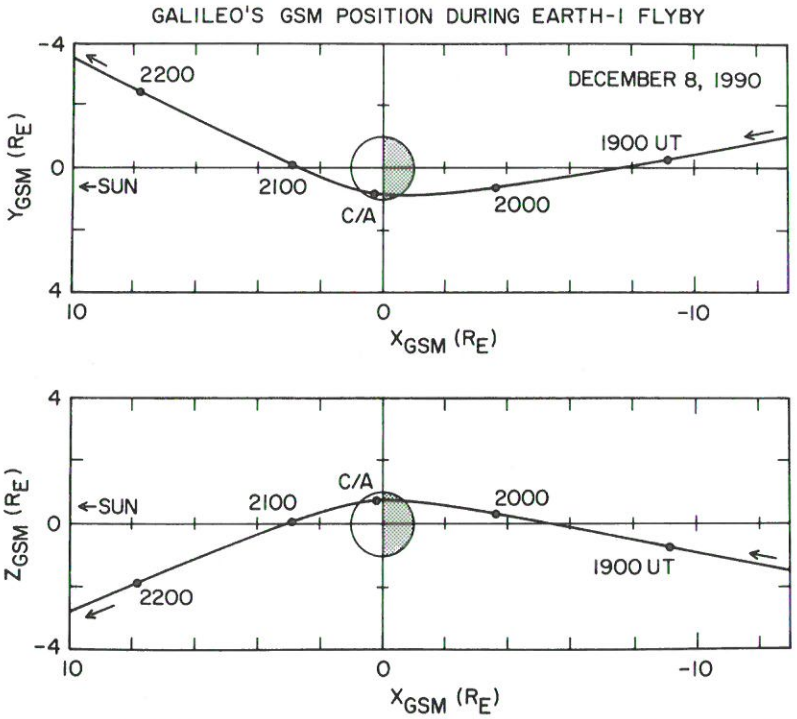

Fig. 1. The Galileo Earth-1 flyby trajectory in Geocentric Solar Magnetospheric (GSM) coordinates, projected into the x–y plane in the top panel and the x–z plane in the bottom panel. The scale is in Earth radii (R_E), and the Earth is represented by the half-shaded circle. Universal Time (UT) is indicated at 1 h intervals along the trajectory

coordinate system is directed toward the Sun, and the magnetic moment of the Earth is in the x–z plane. The y-axis completes the right-handed coordinate system. The top panel shows a projection of the trajectory onto the x–y_{GSM} plane, and the bottom panel shows a projection of the trajectory onto the x–z_{GSM} plane. The vertical and horizontal scales are marked at intervals of 2 R_E. As can be seen, the spacecraft approached the Earth from near local midnight, passed by the Earth at a closest approach altitude of 964 km at 2035 UT, and then departed on the dayside of the Earth at about 1000 LT. This trajectory brought the spacecraft well within the plasmasphere and the ionosphere, where the plasma density is quite high ($>100\,cm^{-3}$) and the magnetic field is relatively strong (>0.1 gauss). It is this region, at geocentric radial distances inside of about 3 R_E, that is of primary interest.

The waves that are the subject of this analysis were detected by the Galileo plasma wave instrument, sometimes abbreviated PWS, which stands for Plasma Wave Subsystem. The plasma wave sensors consist of a 6.6 m tip-to-tip electric dipole antenna, mounted on a boom 10.6 m from the center of the spacecraft body, and a search coil magnetic antenna, mounted on the high gain antenna feed. The locations of these antennas are shown in Fig. 2. Signals from the electric and magnetic antennas are processed by two types of receivers: (1) a step-frequency spectrum analyzer, and (2) a wideband waveform receiver. The step-frequency spectrum analyzer provides low-resolution spectrum measurements from 5.6 Hz to 5.65 MHz and has three frequency ranges. The low-frequency range covers frequencies from 5.62 to 31.1 Hz, the medium-frequency range covers frequencies from 42.1 Hz to 160.8 kHz, and the high-frequency range covers frequencies from 100.8 kHz to 5.65 MHz. The frequency-step pattern of the medium-frequency spectrum analyzer, which is of the greatest interest in this study, is shown in Fig. 3. The low- and high-frequency analyzers have similar frequency step patterns. Note that the frequency sweep is logarithmic (i.e. the logarithm of the frequency increases linearly with time). The low- and medium-frequency analyzers can be connected to either the electric antenna or the magnetic antenna. In the normal mode of operation, these two analyzers cycle back and forth between the electric and magnetic antennas with a cycle time of 37.33 s. Since the upper frequency range of the magnetic search coil antenna does not extend into the frequency range of the high-frequency analyzer, the high-frequency analyzer remains continuously connected to the electric antenna.

The wideband receiver provides high-resolution waveform measurements and has three frequency bands: 5 Hz–1 kHz, 50 Hz–10 kHz, and 50 Hz–80 kHz. The wideband receiver can be connected to either the electric antenna or the magnetic antenna. The frequency band and antenna selection are controlled by command. Waveforms in the selected frequency band are digitized with a 4-bit analog-to-digital converter. Because of the limited dynamic range of the analog-to-digital converter, an automatic gain control is used to insure that the signal amplitude remains within the available dynamic range. The waveforms are sampled in blocks, the duration of which is determined by the receiver bandwidth and rate of data transmission. A typical block, for example in the 50 Hz–10 kHz bandwidth mode at a bit rate of 100.8 kb s^{-1}, consists of 1574 samples taken at a sample rate of 25,200 samples per second. A typical duration between data blocks is $66\frac{2}{3}$ ms. On the ground, each block of waveform data is Fourier trans-

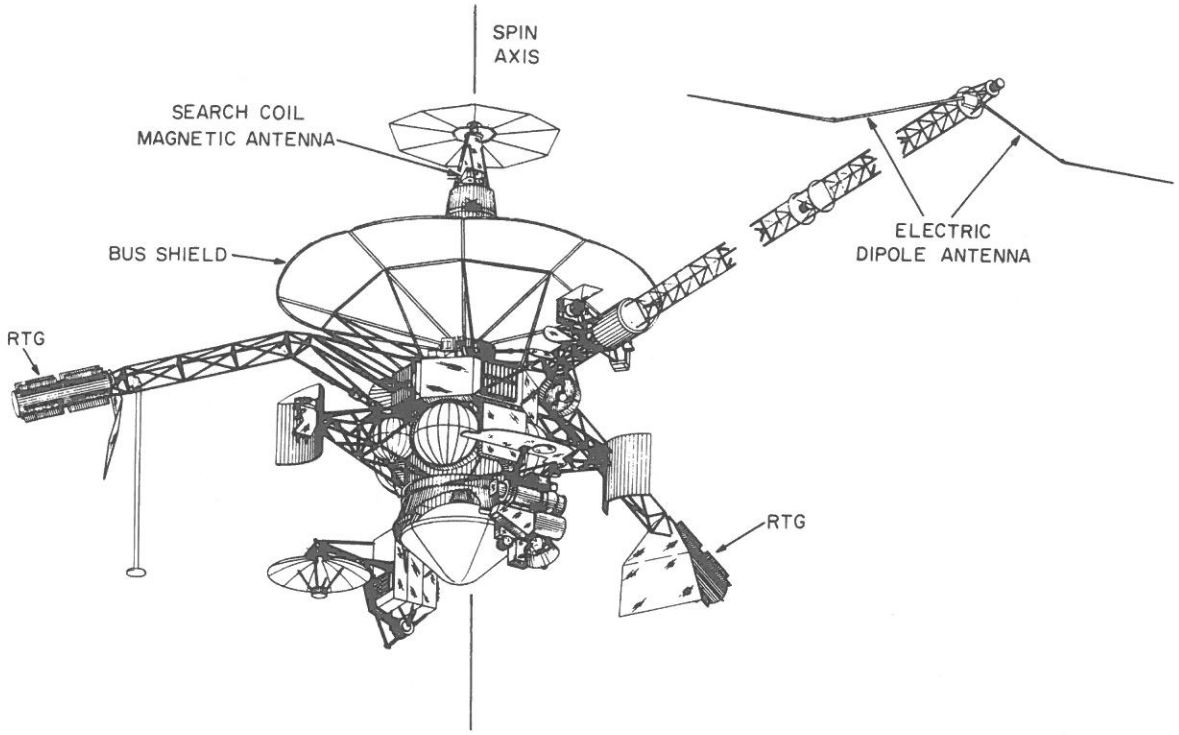

Fig. 2. A drawing of the Galileo spacecraft showing the locations of the electric dipole antenna at the end of the 10.6 m boom, the magnetic search coil antenna, the bus shield, and the Radioisotope Thermoelectric Generators (RTGs). The spacecraft rotates about the vertical line labelled "spin axis"

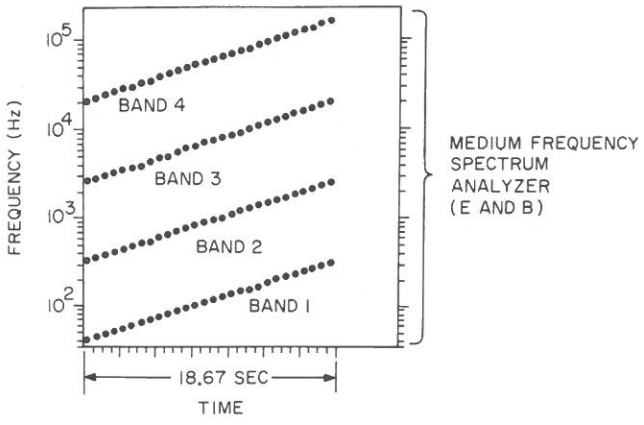

Fig. 3. A diagram showing the scheme for sampling the outputs from the medium-frequency spectrum analyzer channels. The frequency channels are grouped into four bands. The basic sampling cycle is completed in 28 steps, which corresponds to a time interval of 18.67 s (adapted from Gurnett *et al.* (1992))

formed to provide a spectrum. The spectrums from successive data blocks are then assembled into a frequency–time spectrogram, which can be used to study the temporal evolution of plasma wave phenomena on a highly resolved timescale. For further details on the capabilities and operation of the Galileo plasma wave instrument, see Gurnett *et al.* (1992).

3. Observations

A frequency–time spectrogram of the electric field data obtained from the step-frequency spectrum analyzer during the first Earth flyby is shown in Fig. 4. Frequencies are displayed logarithmically on the vertical axis starting at 42.1 Hz and ending at 5.65 MHz, and the time of day in Universal Time (UT) is displayed on the horizontal axis starting at 1930 UT and ending at 2130 UT. The geocentric radial distance to the spacecraft, in Earth radii (R_E), is given at the bottom of the plot. The time and radial distance of closest approach (C/A) are also noted. The electric field spectral density is indicated by the color scale at the top of the figure, and runs from 10^{-17} (blue) to $10^{-10}\,V^2\,m^{-2}\,Hz^{-1}$ (red). The spectrogram in Fig. 4 shows many of the same plasma wave phenomena commonly observed by other spacecraft in the inner regions of the Earth's magnetosphere. These include upper hybrid waves (of the type reported by Walsh *et al.* (1964), Bauer and Stone (1968), Gregory (1969), Hartz (1969), and later studied in more detail by Mosier *et al.* (1973), and others), plasmaspheric hiss (first observed by Russell *et al.* (1969) and later studied in more detail by Thorne *et al.* (1973), Parady and Cahill (1973), and others), and chorus (first described by Storey (1953) and Allcock (1957)).

The upper hybrid emissions, which occur above about 100 kHz in the region near closest approach, provide a convenient method of measuring the plasma density. The upper hybrid resonance frequency is given by $f_{UHR} = \sqrt{f_{pe}^2 + f_{ce}^2}$, where f_{pe} is the electron plasma frequency and f_{ce} the electron cyclotron frequency. Throughout most of the region of interest, $f_{pe} \gg f_{ce}$ so $f_{UHR} \simeq f_{pe}$. Since $f_{pe} \simeq 9\sqrt{n_e}$ kHz, where n_e is the electron density in cm^{-3}, the upper hybrid resonance frequency provides a direct indication of the electron density. As one can see from Fig. 4, the electron plasma frequency, hence electron density, increases abruptly from about 30 kHz

($n_e \simeq 11\,\mathrm{cm}^{-3}$) to 150 kHz ($280\,\mathrm{cm}^{-3}$) at 1956 UT, rises gradually to a peak of about 2 MHz ($4.9 \times 10^4\,\mathrm{cm}^{-3}$) near closest approach at 2035 UT, and then declines slowly to about 120 kHz ($180\,\mathrm{cm}^{-3}$) at 2114 UT, where it abruptly decreases back to about 30 kHz ($11\,\mathrm{cm}^{-3}$). The abrupt changes in the plasma density at 1956 and 2114 UT are characteristic of the entry into and the exit from the plasmasphere. The plasmasphere is a region of relatively cold corotating plasma near the Earth that has a plasma density significantly higher than other regions of the magnetosphere (Carpenter, 1963, 1966).

The plasma wave emissions that are the subject of this study appear in Fig. 4 as a series of stripe-like features in the region near closest approach, from about 2045 to 2100 UT. The stripe-like features sweep upward across the spectrogram, always increasing with increasing time, and are only observed in the electric field data. The maximum electric field strengths are about $100\,\mu\mathrm{V\,m}^{-1}$. The stripes have several unusual characteristics. First, even though the frequency scale is logarithmic, the stripes have a linear relationship between the logarithm of the frequency and time. Second, the slope of the stripes on the log-frequency-versus-time plot is constant, independent of the spacecraft position. Since it is highly unlikely that any naturally occurring magnetospheric phenomena could maintain the same linear log-frequency-versus-time relationship over such a large range of plasma parameters, it is highly unlikely that the stripes are indicative of the true frequency–time variation of the phenomena being detected. Instead, the linear log-frequency-versus-time characteristic suggests that the response is somehow controlled by the step-frequency receiver, which has a linear log-frequency-versus-time sweep.

The linear log-frequency-versus-time characteristics of the stripes can be explained if we assumed the signals causing the stripes are of short duration ($\sim$ a few seconds), have a broad bandwidth, and occur only once per spacecraft rotation. To understand how a brief, broadband, once-per-rotation signal can appear as a series of linear stripe-like features in a frequency–time spectrogram, consider more closely the operation of the medium-frequency spectrum analyzer. As shown in Fig. 3, the medium-frequency spectrum analyzer consists of four bands, each with 28 frequency steps. At any given time in the measurement cycle, one frequency from each band is being sampled. Each sample takes $\frac{2}{3}$ s, so the total time to go through 28 steps is 18.67 s. The spacecraft rotation period during the first Earth flyby was 19.07 s. Thus, the medium-frequency spectrum analyzer makes approximately 29 measurements during each rotation of the spacecraft. Therefore, a "beat" exists between the spacecraft rotation and the cycling of the step-frequency analyzer. A brief, broadband, once-per-rotation signal detected in analyzer steps 3–5 during one rotation would be detected in steps 4–6 during the next rotation, in steps 5–7 during the following rotation, etc. It is easy to show that the beat period, T, required for the stripe to pass through one of the 28-channel bands of the step-frequency analyzer is given by

$$\frac{1}{T} = \left(\frac{1}{18.67\,\mathrm{s}} - \frac{1}{19.07\,\mathrm{s}}\right). \qquad (1)$$

This formula gives a beat period of $T = 890.1$ s, or about 14.8 min. Since 28 channels correspond to a factor of eight in frequency (the full frequency range of the medium-frequency analyzer has $4 \times 28 = 112$ channels), the response on a spectrogram such as Fig. 4 should be linear with a slope of three octaves (a factor of eight) in frequency per 14.8 min. As can be seen in Fig. 4, this slope is in very good agreement with the observed slope. If one broadband burst is detected per rotation then four stripes should be observed at any one time, one for each of the 28-channel bands. As can be seen in Fig. 4, four stripes are usually present at any one time.

To test the beat hypothesis, the wideband waveform receiver measurements obtained during the time interval around closest approach were examined to see if a broadband burst of noise was observed once per rotation. Representative frequency–time spectrograms of the signals from the wideband receiver in the region near closest approach are shown in Figs 5–7. Figure 5 shows the electric field spectral density for an interval of just over 1 min on the inbound leg starting at 2016:16 UT, when Galileo was at a geocentric radial distance of about 2.3 R_E. The frequency scale on the vertical axis of this spectrogram extends from 0 to 10 kHz, and the timescale on the horizontal axis, called Relative Time (RT), extends from 0 to 60 s. Spectral density is plotted on the color scale shown at the top of the figure, and runs from 0 (blue) to 40 dB (red). As can be seen, a band of enhanced emissions can be seen extending across the spectrogram at about 2 kHz. This band has clearly defined intensifications at 14, 33, and 52 s RT. The interval between these intensifications ($\sim$19 s) is almost exactly the spacecraft rotation period. The band of enhanced emission at about 2 kHz is frequently observed in the ionosphere and plasmasphere and is known to be associated with the lower hybrid resonance frequency (see Brice and Smith, 1965; McEwen and Barrington, 1967; Storey and Cerisier, 1968; Gurnett *et al.*, 1969). For a sufficiently dense plasma with a single ion species, the lower hybrid resonance frequency is given by $f_{LHR} = \sqrt{f_{ce} f_{ci}}$, where f_{ce} is the electron cyclotron frequency and f_{ci} the ion cyclotron frequency. At the relatively high altitude (8300 km) where these observations were made, the dominant ion is expected to be H^+. The lower hybrid resonance frequency computed assuming a pure H^+ plasma is shown by the white line in Fig. 5. As can be seen, the band of enhanced emission is centered almost exactly on the lower hybrid resonance frequency. Usually the lower hybrid resonance frequency corresponds to the lower cutoff of the band of enhanced emission. One can see from Fig. 5 that the lower cutoff is a few hundred Hertz below the computed lower hybrid resonance frequency. This slight discrepancy is not surprising since the lower hybrid resonance frequency was computed assuming a pure H^+ plasma. In the plasmasphere, heavier ions, especially O^+, are expected to be present. The presence of these heavier ions causes the lower hybrid resonance frequency to be somewhat lower than for a pure H^+ plasma.

Figure 6 shows another wideband frequency–time spectrogram starting at 2044:40 UT, shortly after closest approach, when Galileo was about at a geocentric radial distance of 1.6 R_E. This spectrogram uses the same color

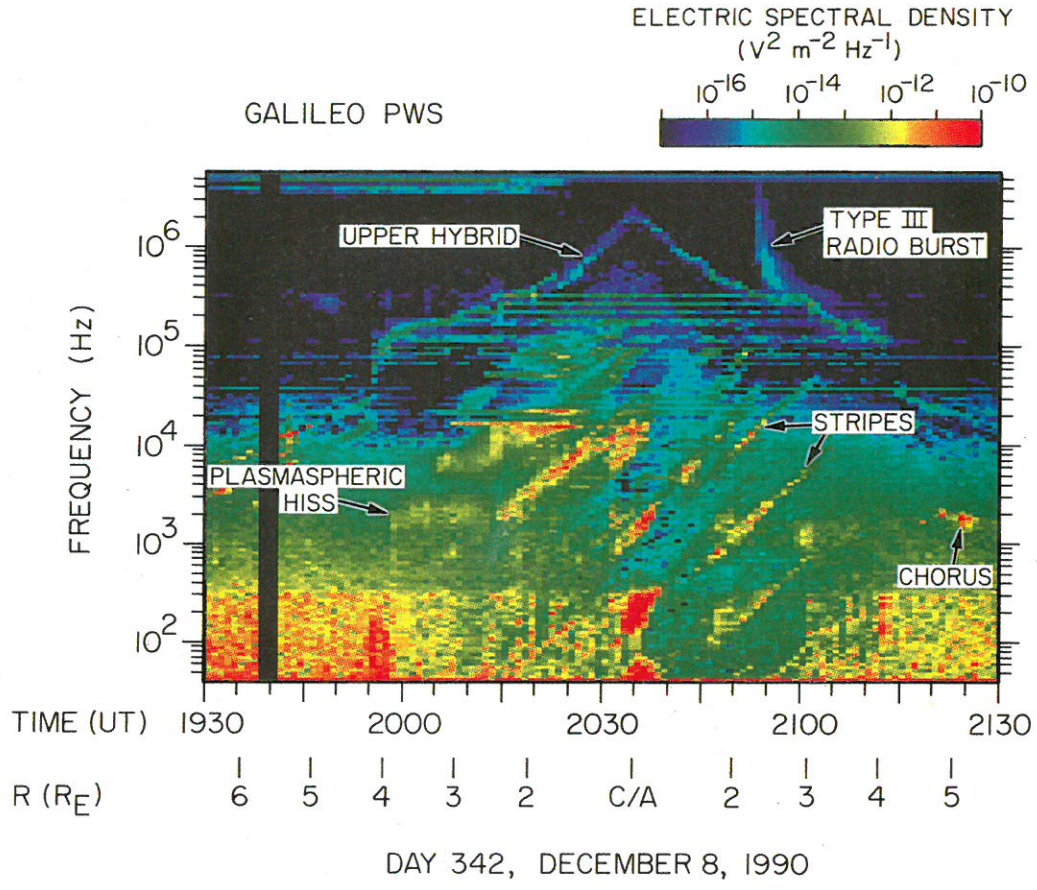

Fig. 4. A frequency–time spectrogram of electric field intensities from the step-frequency receiver during the Earth-1 flyby. The vertical axis shows the frequency in Hertz (Hz) and the horizontal axis shows Universal Time (UT) in hours and minutes. Color indicates the electric field spectral density on a scale from 10^{-17} (blue) to 10^{-10} (red) $V^2 m^{-2} Hz^{-1}$

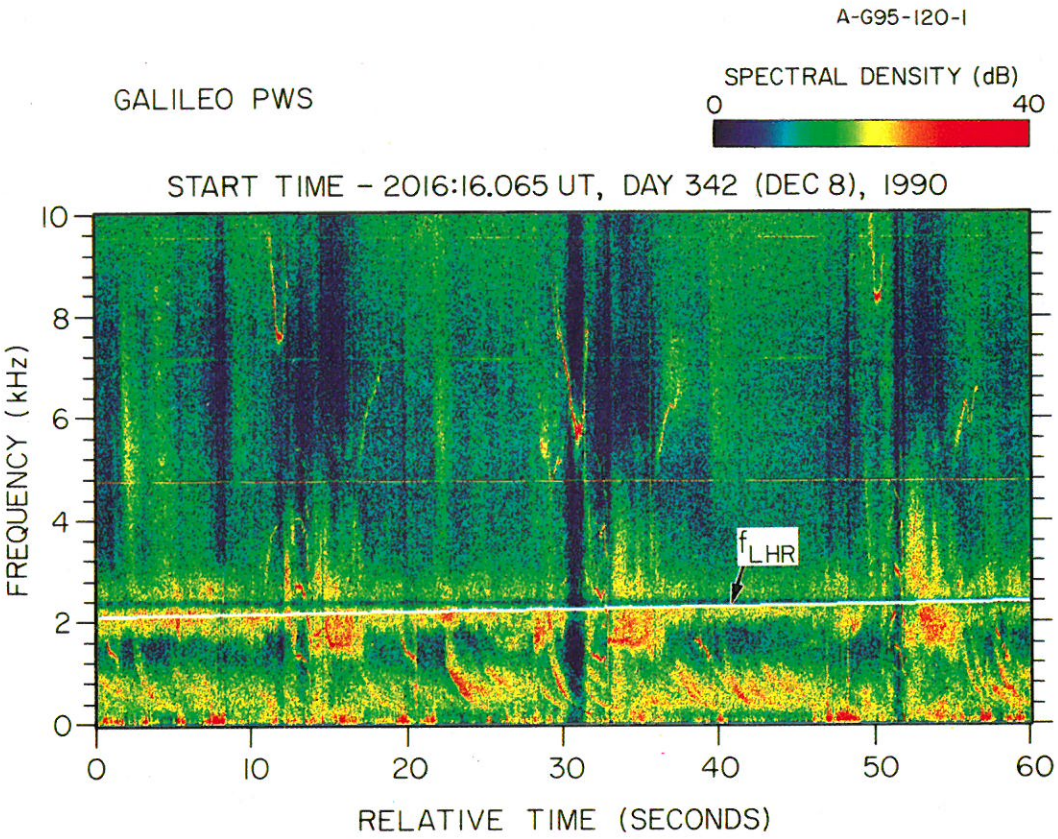

Fig. 5. A wideband frequency–time spectrogram taken well before closest approach. The vertical axis shows frequency in kiloHertz (kHz) and the horizontal axis shows time, called Relative Time, in seconds after 2016:16 UT. The electric field spectral density is shown in color on a scale from 0 (blue) to 40 (red) dB. The lower hybrid resonance frequency is indicated by a white line labelled f_{LHR}

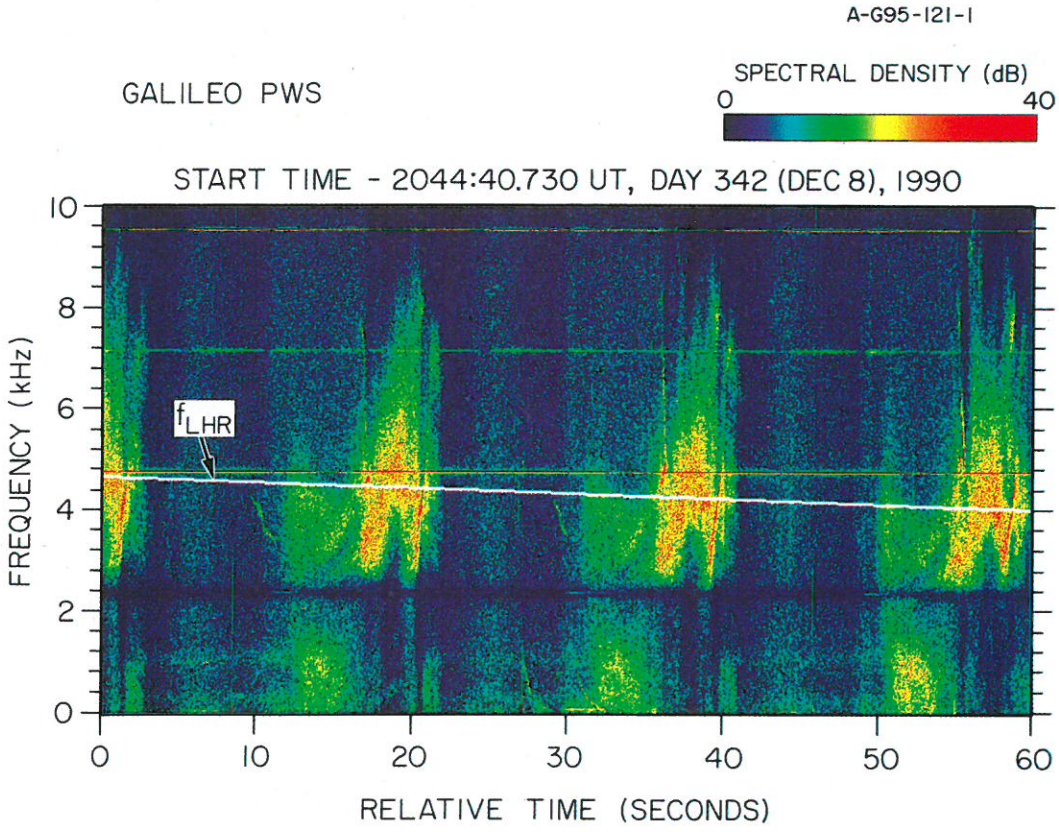

Fig. 6. A wideband frequency–time spectrogram taken shortly after closest approach, displayed in a format similar to Fig. 5. This spectrogram shows a series of clearly defined once-per-spin bursts near the lower hybrid resonance frequency, f_{LHR}. The horizontal lines are interference at harmonics of the spacecraft power system, which operates at a frequency of 2.4 kHz

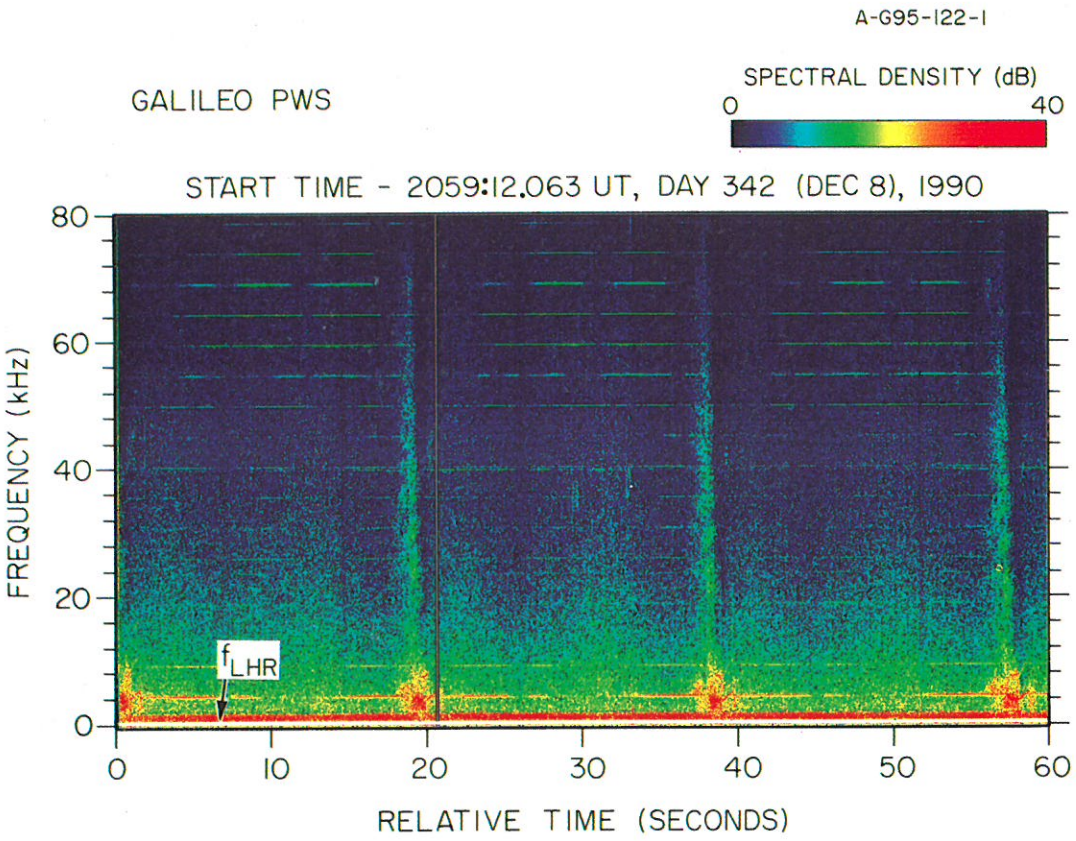

Fig. 7. A wideband frequency–time spectrogram taken well after closest approach in a format similar to Fig. 5. Note that the frequency scale is now 0–80 kHz. This spectrogram shows a series of broadband once-per-spin bursts extending over the entire frequency range. The spectrum of these bursts shows a strong intensification near the lower hybrid resonance frequency, f_{LHR}, which is near the bottom of the spectrogram (white line)

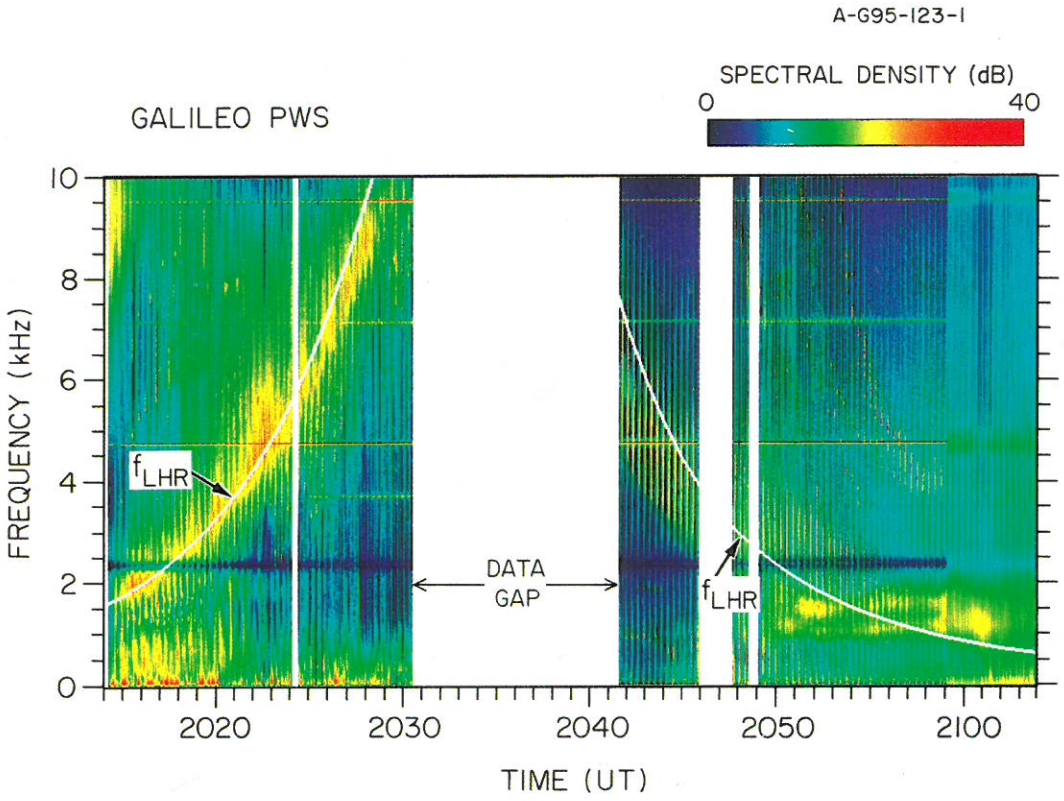

Fig. 8. A wideband frequency–time spectrogram similar to Figs 5–7, but with the timescale compressed to show all of the wideband data in the region around closest approach, from 2014 to 2104 UT. The once-per-spin bursts appear as a series of closely spaced vertical spikes. The spectrum of these spikes has a clearly defined enhancement near the lower hybrid frequency, f_{LHR}, which is shown by the white line

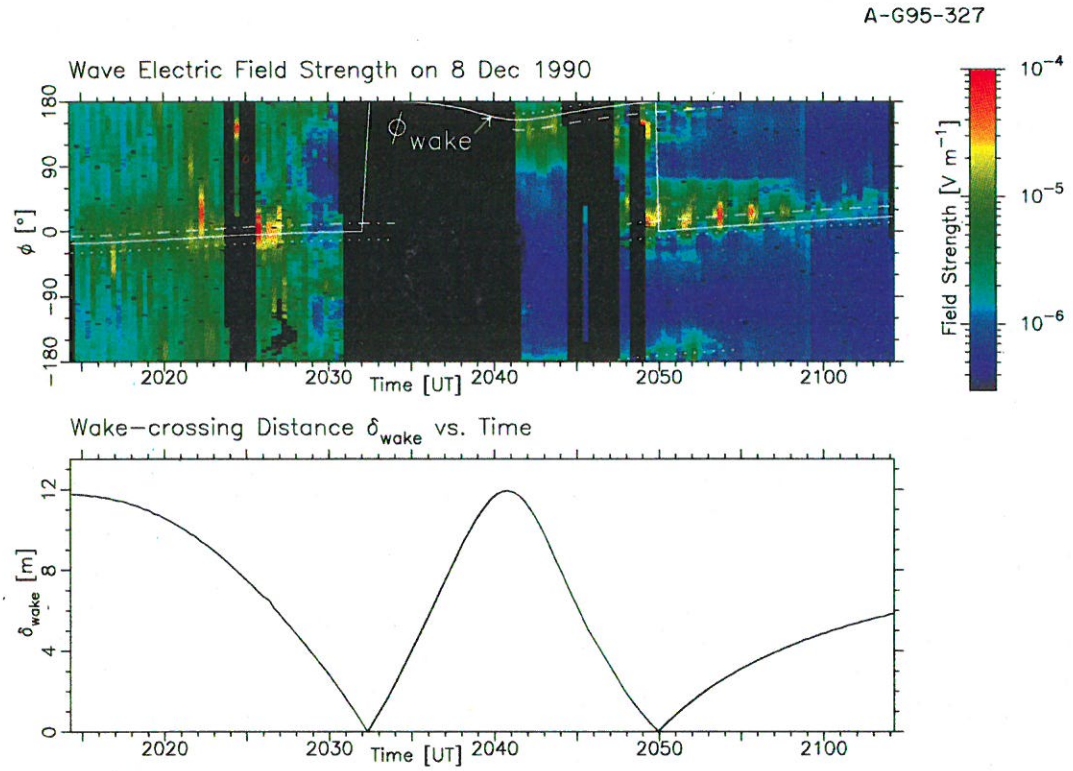

Fig. 11. The spectrogram in the top panel shows the broadband electric field strength as a function of the spacecraft rotation angle ϕ and time. The white line labelled ϕ_{wake} gives the rotation angle at which the magnetic field line through the electric antenna intersects the wake axis. A clearly defined enhancement occurs when $\phi \simeq \phi_{wake}$. The bottom panel shows the distance parameter, δ_{wake}, as a function of time. The discontinuities in ϕ_{wake}, at 2032:20 and 2049:50 UT, occur as the magnetic field passes through the spin plane. Note that $\delta_{wake} = 0$ at these times

scale and frequency–time axes as Fig. 5. In this case, a very strong once-per-rotation modulation can be seen, with bursts at 18, 37, and 56 s RT, again centered on the lower hybrid resonance frequency. The lower hybrid resonance frequency (computed assuming a pure H^+ plasma) is shown by the white line. Figure 7 shows another example of the once-per-rotation bursts at about 2059:14 UT, when Galileo was at a radial distance of about 2.9 R_E on the outbound leg. The electric field spectral densities are again displayed using the same color scale and format as Fig. 5, except that the frequencies now extend from 0 to 80 kHz. As can be seen, a series of broadband bursts appears at ~19, 38, and 57 s RT. The time interval between these bursts is almost exactly the spacecraft spin period. The bursts have a very broad bandwidth, with frequencies extending from near the lower hybrid frequency, which is at about 1 kHz, to as high as 60 kHz. As in the previous examples, the highest intensities occur near the lower hybrid resonance frequency.

An examination of all the wideband spectrograms recorded during the first Earth flyby shows two periods where a strong once-per-spin modulation appeared, the first from 2014 to 2031 UT, and the second from 2041 to 2104 UT. These two intervals are separated by a data gap from about 2031 to 2041 UT. Since the stripe-like features were observed in the step-frequency receiver through the gap in the wideband data, it is likely that the once-per-spin bursts occurred continuously over the entire interval from 2014 to 2104 UT. The frequency spectrum of the signals detected by the wideband receiver through the entire pass is summarized in Fig. 8. This spectrogram is similar to Fig. 5, but the timescale has been compressed so that the entire interval from 2014 to 2104 UT is displayed. As can be seen, the electric field spectrum has a well-defined enhancement at a frequency that closely tracks the lower hybrid resonance frequency, shifting steadily upward in frequency on the inbound pass, from about 2 kHz at 2015 UT to about 10 kHz at 2028 UT, and shifting steadily downward in frequency on the outbound pass, from about 6 kHz at 2042 UT to about 1.5 kHz at 2055 UT. The vertical spike-like features evident on a fine timescale (~19 s) are caused by the once-per-rotation modulation.

4. Origin of the rotational modulation

It is well known that the response of an electric dipole antenna rotating in a constant amplitude wave field has a characteristic twice-per-rotation modulation. The maximum response occurs when the axis of the antenna is parallel to the electric field, and the minimum response occurs when the antenna is perpendicular to the electric field. As the spacecraft rotates, the antenna axis passes through perpendicular twice each rotation, which gives rise to the characteristic twice-per-rotation modulation. For wavelengths long compared to the length of the antenna, it is easy to show that the intensity varies as $\cos^2\theta$, where θ is an angle that characterizes the rotational orientation of the antenna. Since the Galileo electric antenna is mounted on the end of a long boom, the antenna essentially acts as a probe that surveys the wave intensity in a circular arc around the spacecraft. The fact that only one peak occurs per rotation can mean either that the waves are generated only during a certain phase of the spacecraft rotation, or that the waves are generated continuously, but are confined to a localized beam that is traversed once per rotation. In either case, the once-per-rotation modulation implies that waves must be generated in the near vicinity of the spacecraft. The key issues then have to do with the location of the source, the mode of propagation, and the mechanism by which the waves are generated.

In the process of carrying out this study, several models were considered to explain the once-per-rotation modulation. These include: (1) electrical discharges produced by spacecraft charging effects, (2) instabilities produced by pick-up ions from propellant leaks or other unknown gas sources, and (3) instabilities generated in the plasma wake of the spacecraft. Of these, the plasma wake model provides a source that is consistent with all of the available observations. The remainder of this section is devoted to a discussion of this model, which is called the wake source hypothesis.

4.1. *The wake source hypothesis*

Since the emissions are strongest near the lower hybrid resonance frequency, there are good reasons to believe the waves are propagating in the lower hybrid mode. The lower hybrid mode is a limiting case of the whistler mode (Stix, 1962). For frequencies near the lower hybrid resonance, the wavelengths become very small at wave normal angles near the resonance cone and the fields become electrostatic. An important property of the lower hybrid mode is that the wave energy (i.e. the group velocity) is guided very nearly along the magnetic field. For a discussion of this guiding effect, see Mosier and Gurnett (1969). Since lower hybrid waves are guided very closely along the magnetic field, a simple test can be performed to determine if the source is located in the downstream wake region. If the waves are generated in the wake, then the maximum intensities should occur when the magnetic field through the electric antenna intersects the wake. The geometry involved is illustrated in Fig. 9. Note that as the spacecraft rotates there is only one orientation that produces a magnetic connection between the center of the electric antenna and the wake axis. Thus, there should be only one peak per rotation, which is the defining characteristic of the stripe-like emissions.

To carry out a quantitative test of the wake source hypothesis, a suitable coordinate system must be used to analyze the spin modulation. For this purpose, it is convenient to define a rotation angle, ϕ, which is the angle between the boom that carries the electric dipole antenna and the projection, $\vec{B}_\perp$, of the magnetic field onto a plane perpendicular to the spin axis. This angle is measured positive from the magnetic field in the direction of rotation. At some phase of the rotation, $\phi = \phi_{wake}$, the magnetic field line through the center of the antenna intersects the wake axis. The geometry at this instant in time

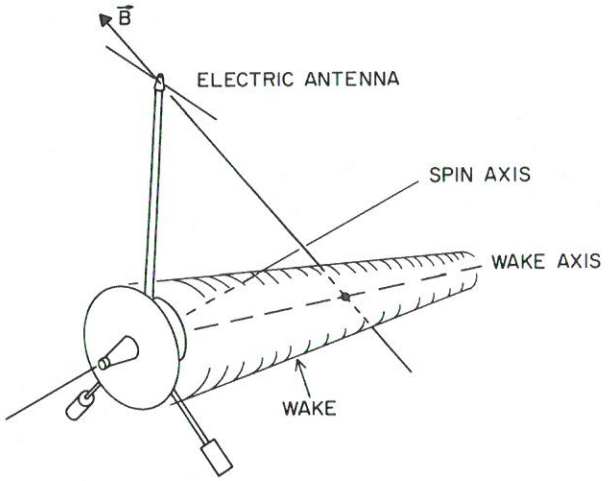

Fig. 9. A sketch showing a magnetic field line linking the electric antenna to the spacecraft wake. The black dot indicates the intersection of this magnetic field line and the wake axis. Since the spacecraft velocity vector usually makes a substantial angle relative to the spin axis, the wake axis is in general not coincident with the spin axis

is illustrated in Fig. 10. The top panel shows a view looking along the spin axis, and the bottom panel shows a view looking perpendicular to the spin axis. In general, the wake axis is not aligned along the spacecraft spin axis, so the magnetic field-to-wake intersection is offset to one side as shown in the top panel. To determine the orientation of the wake axis, it is necessary to compute the spacecraft velocity, $\vec{V}_{s/c}$, relative to the plasma. The computation of $\vec{V}_{s/c}$ must take into account the fact that the plasma within the plasmasphere corotates with the Earth. From knowledge of the wake axis orientation, the spin axis orientation (which was directed toward the Sun), and the magnetic field direction, it is a straightforward matter to compute the angle ϕ_{wake}. Since the downstream location of the intersection is also potentially important, the distance δ_{wake} at which the magnetic field line intersects the wake axis was also computed. This distance is measured along the wake axis from the center of the spacecraft body as shown in the bottom panel of Fig. 10.

To compare the observations with the predictions of the wake source hypothesis, a spectrogram display was developed that shows the broadband electric field strength as a function of the spacecraft rotation angle, ϕ, and time. A spectrogram of this type is shown in the top panel of Fig. 11. The vertical axis gives the rotation angle in degrees, and the horizontal axis gives the time in UT using the same scale as in Fig. 8. The color at any given point in the spectrogram shows the electric field strength, which runs from 3×10^{-7} (blue) to 10^{-4} V m^{-1} (red). The electric field strength was calculated from the wideband receiver data. To restrict the response to the part of the spectrum where the once-per-rotation modulation is the strongest, and to suppress unwanted magnetospheric emissions, the electric field strength was computed by integrating the wideband spectrums from 1 to 9 kHz. As described earlier, one wideband spectrum can be computed from each 66.7 ms data block. Since the wideband receiver has an automatic gain control (AGC), it was also necessary to take into account variations in the AGC gain. The AGC

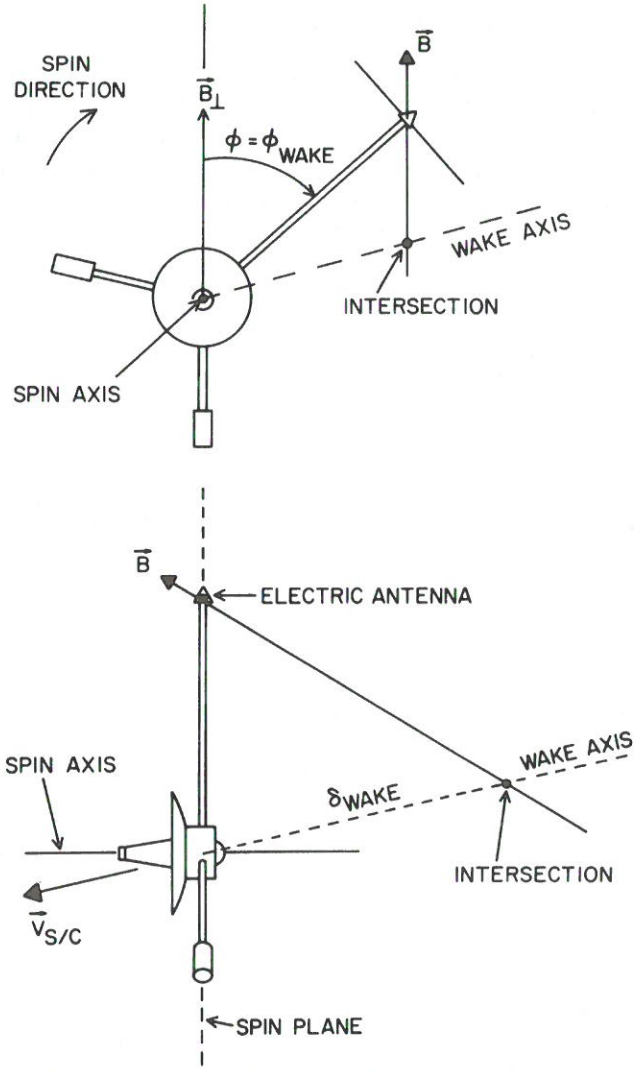

Fig. 10. Two views, looking parallel and perpendicular to the spin axis, showing the geometry at the time that the magnetic field line through the antenna intersects the wake axis. The rotation angle ϕ is defined as the angle between the electric antenna boom and the pojection, $\vec{B}_{\perp}$, of the magnetic field onto the spin plane. At the time of intersection, $\phi = \phi_{wake}$. The parameter δ_{wake} is the distance from the center of the spacecraft body to the intersection of the magnetic field line and the wake axis

gain is sampled once every 2.67 s and has a time constant of 0.1 s. To provide AGC gain values on a timescale consistent with the 0.0667 s spectrum integration interval, the AGC gain was interpolated between the 2.67 s samples using a spline routine. Using this procedure a total of approximately 287 electric field strength values were obtained per spacecraft rotation. These values were then used to generate one vertical line in the spectrogram, thereby giving a time resolution corresponding to one rotation, or about 19 s. As can be seen, the peak broadband electric field strength of the spin modulated noise is about 10^{-4} V m^{-1}.

In Fig. 11, the rotational angle, ϕ_{wake}, at which the magnetic field line through the center of the electric antenna intersects the wake axis, is indicated by the solid white line. The meaning of the adjacent dotted and dot-dashed

lines is explained in the next section. As can be seen, the peak in the rotational modulation closely follows the wake-intersection line. The abrupt 180° discontinuity in ϕ_{wake} at 2032:20 UT, and again at 2049:50 UT, occurs as the magnetic field passes through the spin plane. Note that δ_{wake} goes to zero at these two times. Considerable scatter exists in the electric field strengths on the left-hand side of the spectrogram, with peaks sometimes occurring at random angles. Inspections of the wideband spectrograms during this interval show that these random peaks are caused by whistlers, chorus, and other naturally occurring magnetospheric emissions. On the right-hand side of the spectrogram, the scatter is much smaller with one main peak that closely tracks the wake-intersection line. Overall, the close agreement between the angular location of the once-per-rotation peak and the wake-intersection line gives strong support for the wake source hypothesis.

4.2. *The angular spread of the modulation pattern*

It is evident from the spectrogram in Fig. 11 that the peak in the modulation pattern extends over a considerable range of angles, on the order of $\Delta\phi \simeq 30$–$40°$. At the center of the electric antenna, which as previously described traces out a circular arc around the spacecraft body, this angular spread corresponds to an arc length of about 6 m. Several factors have been considered that could in principle contribute to this angular spread. These include: (1) the beamwidth relative to the magnetic field, (2) the finite wavelength and antenna length, and (3) the finite diameter of the wake. Each of these factors is now considered in detail.

4.2.1. *Beamwidth.* For lower hybrid waves, the wave energy propagates in a cone of directions around the magnetic field that is determined by the resonance cone angle. For frequencies near the lower hybrid resonance frequency, it is easily shown (Gurnett *et al.*, 1979) that the angle, ψ, between the direction of energy propagation (group velocity) and the magnetic field is given to a good approximation by the equation

$$\tan^2\psi = \frac{f^2 - f_{LHR}^2}{f_{ce}^2} \tag{2}$$

where f is the wave frequency, f_{LHR} the lower hybrid resonance frequency, and f_{ce} the electron cyclotron frequency. This equation is valid in the high-density limit, $f_{pe}^2 \gg f_{ce}^2$, a condition that is usually satisfied in the region of interest. For $f = f_{LHR}$, the above equation shows that the wave energy is guided exactly along the magnetic field ($\psi = 0$). Since $f_{ce}^2 \gg f_{LHR}^2$, one can see that ψ is small even if f is substantially greater than f_{LHR}. For example, if $f = 2f_{LHR}$, $\psi \simeq 2.3°$, and if $f = 5f_{LHR}$, $\psi \simeq 6.5°$. These calculations show that the beaming angles are much smaller than the observed angular spread, so finite beamwidth effects do not play a role in determining the angular spread of the modulation pattern.

4.2.2. *Wavelength and antenna length.* It is well known that the transverse width of a beam of radiation cannot be smaller than the wavelength of the waves that make up the beam. The fact that the spin-modulated emissions are confined to a small arc (~ 6 m) of the antenna motion shows that the wavelengths must be quite small, not more than a few meters. On the other hand, the wavelengths cannot be too small, because the antenna would then not respond to the electric field. For a cylindrical dipole antenna of the type used on Galileo, it is easily shown that the antenna response (received intensity/incident intensity) varies as $(\sin x/x)^4$, where $x = \pi(L/2)/\lambda$, L is the tip-to-tip length of the antenna, and λ the wavelength (Fuselier and Gurnett, 1984). Although the exact ratio of the incident intensity to the received intensity is not known, one can see from the above equation that the antenna response decreases very rapidly for the wavelengths less than about $L/2$. Since $L/2$ for the Galileo antenna is approximately 3.3 m, the wavelengths probably cannot be much less than 1 m, and almost certainly cannot be as small as 0.1 m.

4.2.3. *Wake diameter.* Since the spacecraft body has a finite size, it is clear that the wake cannot be simply represented by a line as was done in Figs 9 and 10. To take into account the finite size of the wake, one must consider the geometry of the wake. For an initial evaluation, we adopt a simple model. This model assumes that the spacecraft sweeps out a cylindrical "hole" in the plasma downstream of the spacecraft, the diameter of which is determined by the transverse dimensions of the spacecraft body. The largest object on the spacecraft body is the bus shield (see Fig. 2), which has a diameter of 4.2 m. The diameter of the wake is therefore taken to be 4.2 m. In general the wake axis is not aligned along the spacecraft spin axis, so the wake would appear as shown in Fig. 12.

To compare the spin modulation pattern with the cylindrical wake model, dotted and dot-dashed lines are shown in Fig. 11 that represent the rotation angles at which the magnetic field line through the center of the antenna intersects the boundaries of a cylindrical wake. The same dotted and dot-dashed coding is used in both Figs 11 and 12. As can be seen, the rotation angle from wake entry to wake exit is typically about 30°. This angular width, from wake entry to exit, is somewhat smaller than the angular spread of the modulation pattern. Most likely this disagreement is due to the finite wavelength and finite antenna length effects discussed earlier, both of which would act to increase the effective angular spread relative to what one would expect for a simple cylindrical wake.

Because of thermal motions in the plasma, the wake probably does not have the simple cylindrical configuration described above, but rather closes in a conical configuration downstream of the spacecraft (Katz *et al.*, 1985). The half-angle of the wake cone is given by $\tan^{-1}(v_i/V_{s/c})$, where v_i is the thermal speed of the ions and $V_{s/c}$ the spacecraft speed relative to the plasma. If the ions are H^+ at a temperature of about 3000 K, which is typical for the upper levels of the Earth's ionosphere, the half-angle of the wake cone should be approximately 20°. For this half-angle the wake cone would extend about 6.5 m downstream of the spacecraft. For heavier ions, such as O^+, which are more abundant at lower altitudes, the half-angle would decrease by a factor of four, to about 5°,

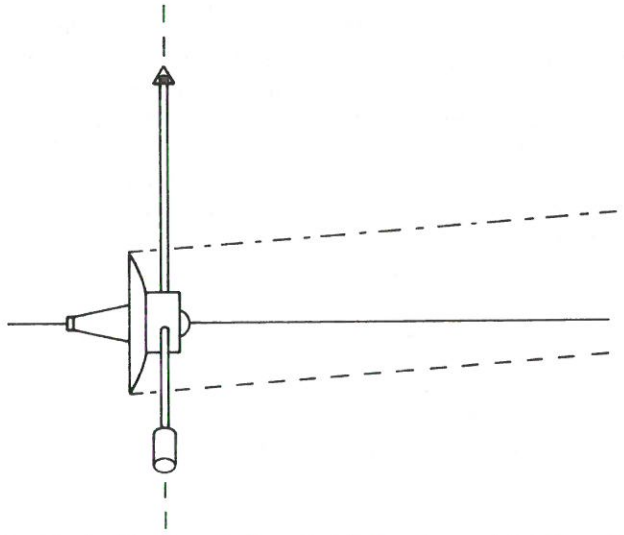

Fig. 12. A side view of the cylindrical wake model. The wake axis in this case has been inclined to the spin axis (horizontal line) by 4.5°. The wake boundaries are indicated by the dotted and dot-dashed lines. The dotted and dot-dashed white lines in the top panel of Fig. 11 correspond to rotation angles at which the wake boundaries intersect the magnetic field line through the electric antenna

which means that the wake cone could then extend as much as 26 m downstream of the spacecraft. These estimates of the downstream dimensions of the wake are generally consistent with the range of δ_{wake} values that occurred during the flyby. As can be seen from Fig. 11, the magnetic field variations were such that the maximum distance δ_{wake} to the downstream wake intersection was about 12 m.

Since the wake is expected to have a conical configuration, it is interesting to see if any evidence of this conical shape exists in the spin modulation pattern. As the distance δ_{wake} to the magnetic field intersection increases, the angular spread in the modulation pattern should decrease. The largest variations in the wake-intersection distance, δ_{wake}, occurred on the inbound leg (see the bottom panel of Fig. 11), so this region should provide the best opportunity to look for evidence of a conical configuration. Unfortunately, on the inbound leg the spin modulation pattern is extremely noisy, which makes it extremely difficult to judge whether the angular spread varies as one would expect. On the outbound leg, the signal-to-noise ratio is much better. As can be seen from Fig. 11, the angular spread in the modulation pattern decreases systematically as δ_{wake} increases, from about 50° at 2050 UT (where $\delta_{\text{wake}} = 0$ m) to about 25° at 2103 UT (where $\delta_{\text{wake}} = 5.8$ m). This variation is consistent with the expectations for a conical wake. However, it should be noted that various other parameters, such as the plasma density and magnetic field, also change significantly over this interval, so one cannot be certain that the wake geometry is the only factor that affects the angular spread.

4.3. *Offset from the wake axis*

From Fig. 11 it is evident that the peak in the spin modulation pattern has a systematic offset relative to the wake intersection angle. On the inbound leg, before 2032:20 UT, where the first 180° discontinuity in ϕ_{wake} occurs, the offset of the peak relative to the wake axis is positive, approximately +10°. From 2032:20 to 2049:50 UT, between the two 180° discontinuities in ϕ_{wake}, the offset is negative, approximately −15°. On the outbound leg, after 2049:50 UT where the second 180° discontinuity occurs, the offset again becomes positive, approximately +15°. These offsets are much larger than can be accounted for by the known integration times and the estimated errors in the attitude determination. For example, the spectrum integration time for one block of wideband data is 66.7 ms, which corresponds to only 1.3° of angular rotation. The errors in the spacecraft attitude determination are expected to be a small fraction of one degree. The fact that the sign of the offset switches in synchronism with the 180° discontinuities in ϕ_{wake} also strongly indicates that the offset is due to a real asymmetry and not due to some gross error in the spacecraft attitude determination. Since the 180° phase shift in ϕ_{wake} occurs as the magnetic field passes through the spin plane, one can see from fairly simple geometric considerations that the synchronism between the change in sign of the offset and the 180° phase shift in ϕ_{wake} means that in both cases the waves are generated on the same side of the wake. To determine which side of the wake is involved, refer to Fig. 10, which corresponds to the configuration before 2032:20 UT and after 2049:50 UT, when the offset was positive. As can be seen, a positive offset corresponds to a source located on the $-\vec{V}_{s/c} \times \vec{B}$ side of the wake. From the length of the boom (10.6 m), it is easy to show that a 10–15° offset corresponds to a physical displacement of the source by about 1.8–2.7 m from the central axis of the wake (toward the $-\vec{V}_{s/c} \times \vec{B}$ direction). Possible reasons for this offset are discussed in the next section.

5. Generation mechanism

Since we have established that the once-per-rotation bursts of electric field noise originate in the plasma wake downstream of the spacecraft, we next investigate possible instabilities that might account for the generation of this noise. Since the emissions are strongest near the lower hybrid resonance frequency, and since the wake is expected to have strong plasma density gradients, one obvious possibility is the lower-hybrid-drift instability (LHDI). Three criteria must be satisfied for the electrostatic LHDI to occur. These criteria are: (1) the existence of a cross-field particle drift and a diamagnetic drift (Krall and Liewer, 1971; Gladd, 1976; Davidson *et al.*, 1977; Huba *et al.*, 1978), (2) a low plasma beta (see Yoon *et al.* (1994) and references therein), and (3) a weak or negligible magnetic shear (Krall, 1977). All three of these conditions are satisfied in the downstream wake. The lower-hybrid-drift instability involves the lower hybrid wave, with a frequency given by $\omega = \omega_{\text{LHR}}$, and a drift wave, with a frequency given by $\omega = k_y v_G$, where v_G is a cross-field particle drift velocity. The lower hybrid and drift waves are coupled by plasma density gradients (Krall

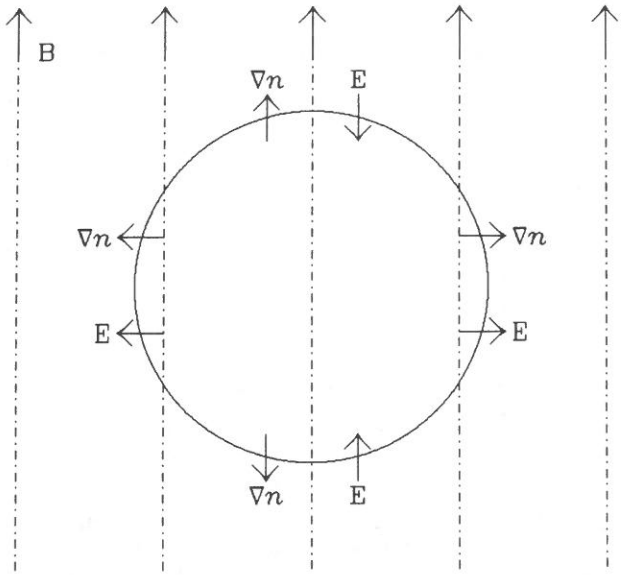

Fig. 13. A diagram depicting the fields and plasma gradients expected near the boundaries of the wake. The circle represents a cross-section of the wake perpendicular to the wake axis, while the ambient magnetic field $\vec{B}$, the plasma gradient ∇n, and the local ambipolar electric field $\vec{E}$, both parallel and transverse to the magnetic field, are shown

and Liewer, 1971), which provide the free energy source for the instability. The origin of this coupling can be seen heuristically from the equation (see equation (7) of Krall and Liewer (1971))

$$(\omega - k_y v_E)(\omega - \omega_{\mathrm{LHR}}) = -\frac{k_y v_{\mathrm{dr}}}{k^2 \lambda_{\mathrm{D}}^2} \frac{\omega^2}{\omega_{\mathrm{pi}}^2} \tag{3}$$

where ω is the wave frequency, k the wave number, ρ_e the (thermal) electron gyroradius, λ_D the Debye length, v_E the $\vec{E} \times \vec{B}$-drift speed, and v_{dr} the diamagnetic drift speed. In this equation, the z-axis is along the magnetic field, the x-axis is along the density gradient, and the y-axis completes the right-handed coordinate system. It is also assumed that the wave vector is perpendicular to the magnetic field, $k_z = 0$, that the electron gyroradius is much smaller than the wavelength, $k_y^2 \rho_e^2 \ll 1$. Instability occurs whenever the right-hand side of equation (3) is non-zero.

It is useful to consider qualitatively the mechanism of ambipolar electric field generation in the satellite wake, illustrated schematically in Fig. 13. The dynamics in the depletion region (represented by the circle in Fig. 13) is different in the directions parallel and transverse to the magnetic field. Parallel to the magnetic field, the electrons tend to fill the depletion faster than the ions because of the larger electron thermal speed. An ambipolar electric field that opposes this tendency is set up and is directed into the depletion region. The plasma then flows parallel to the magnetic field at roughly the ion thermal speed. Transverse to the magnetic field, the ions, because of their larger Larmor radius, tend to fill the depletion faster than the electrons. An ambipolar electric field opposing the ion flow is then set up, directed out of the depletion region. In this case, the plasma flows into the depletion at the perpendicular electron diffusion speed. The LHDI, which is excited when $v_E v_{dr} > 0$ (Krall and Liewer, 1971), occurs in the depletion region due to the ambipolar electric field determined by dynamics transverse to the magnetic field.

In the region where the once-per-rotation bursts were observed, the ionospheric plasma has the following approximate parameters: $T_e \approx T_i \approx 3000\,\mathrm{K}$, $n_e \approx n_i \approx 2.0 \times 10^{11}\,\mathrm{m}^{-3}$, and $B \approx 10^{-5}$–$10^{-4}\,\mathrm{T}$. In the rest frame of the spacecraft, the plasma streaming velocity is $v_p \approx 10^4\,\mathrm{m\,s}^{-1}$. From the above parameters, the electron and ion thermal velocities are inferred to be $v_e \approx 2 \times 10^5\,\mathrm{m\,s}^{-1}$ and $v_i \approx 5 \times 10^3\,\mathrm{m\,s}^{-1}$, respectively. The plasma beta is also very low, of the order 10^{-4}–10^{-2}, which justifies the use of the electrostatic approximation.

To derive the appropriate analytical dispersion equation, we proceed by assuming the magnetic field is constant, neglecting spatial variations of the geomagnetic field over the scale of the Galileo spacecraft. One can also assume that the ambient plasma outside the wake is spatially uniform. However, a strong density gradient is expected to occur near the wake boundary. The scale length of this density gradient is defined to be $L_n \equiv -\mathrm{d}(\ln n_e)/\mathrm{d}x$. In the absence of detailed information on the density profile across the wake, the characteristic spatial scale for this density variation is taken to be of the order of the dimension of the satellite, $L_n \sim 1\,\mathrm{m}$. (Another possible estimate is due to Peter *et al.* (1983), who report a plasma penetration depth of the order of $\sqrt{\rho_e \rho_i}$, which is a hybrid of the electron and ion Larmor radii. For the conditions in the plasmasphere, one has $\rho_i \simeq 5\,\mathrm{m}$ and $\rho_e \simeq 0.1\,\mathrm{m}$, so that $L_p \approx 0.75\,\mathrm{m} \sim L_n$.) Assuming that the density gradient is along the x-direction, the diamagnetic drift velocity associated with this density gradient is along the x-direction, the diamagnetic drift velocity associated with this density gradient is along the y-direction and can be estimated by $v_{dr} \simeq kT/(eBL_n)$, which is roughly 10^3–$10^4\,\mathrm{m\,s}^{-1}$. Furthermore, assuming that the potential energy associated with the ambipolar electric field is approximately 10% of the electron thermal energy, the $\vec{E} \times \vec{B}$-drift speed is estimated to be on the order of $10^3\,\mathrm{m\,s}^{-1}$.

Since we are considering waves with frequencies near the lower hybrid resonance frequency, it follows that $\omega_{ci} \ll \omega \ll \omega_{ce}$. Therefore, we can treat the electrons as magnetized and the ions as unmagnetized. Neglecting temperature and magnetic field gradients, the following dispersion equation can be used to describe the electrostatic LHDI (Krall and Liewer, 1971):

$$k^2 \lambda_{\mathrm{D}}^2 = -\frac{T_e}{T_i}\left[1 + \frac{\omega}{k v_i} Z\left(\frac{\omega}{k v_i}\right)\right] - 1 + \frac{m_e}{T_e \pi^{1/2} v_e} \int_{-\infty}^{\infty} \mathrm{d}v_z$$

$$\times \int_0^{\infty} \mathrm{d}v_\perp\, v_\perp J_0^2\left(\frac{k_\perp v_\perp}{\omega_{ce}}\right) \exp\left(-\frac{v_\perp^2 + v_z^2}{v_e^2}\right) \left[\frac{\omega - \dfrac{k_y T_e}{m_e \omega_{ce}} \varepsilon'}{\omega - k_y v_E - k_z v_z}\right] \tag{4}$$

where $\varepsilon' = -\mathrm{d}(\ln n_e)/\mathrm{d}x - E/T_e$, $v_E = -E/B$, and $Z(\xi)$ is the plasma dispersion function. Integrating over velocity space and assuming $T_e \simeq T_i$, we obtain

the spacecraft frame of reference, corrections must be made in the real part of the frequency for the Doppler shift between the two frames of reference. The Doppler shift is given by $\Delta f = (V_{s/c}/\lambda)\cos\Theta$, where λ is the wavelength and Θ the angle between the wave vector $\vec{k}$ and the spacecraft velocity vector $\vec{V}_{s/c}$. Since $V_{s/c} \simeq 11$–$14\,\mathrm{km\,s^{-1}}$ and $\lambda \simeq 1$–$5\,\mathrm{m}$, the Doppler shift can be substantial, $\Delta f \simeq 2$–$14\,\mathrm{kHz}$. The large Doppler shift may account for the broad bandwidth of the once-per-rotation bursts. The main difficulty in evaluating the Doppler shift is the $\cos\Theta$ factor. The conical configuration of the wake and the associated refraction effects are likely to cause significant variations in the wave vector direction as the wave grows and finally escapes from the wake cavity. To fully investigate the effects of the Doppler shift on the emitted frequency requires detailed ray-tracing calculations. At the present state of investigation, such a detailed level of analysis has not been attempted.

Since we have made a strong case that lower hybrid waves can be produced in the plasma wake of a moving spacecraft, the question naturally arises whether lower hybrid waves observed by other Earth-orbiting spacecraft could be caused by similar effects. The specific feature that allowed us to conclude that the waves are generated in the spacecraft wake was the mounting of the electric antenna on a boom well away from the spacecraft body. This mounting configuration resulted in the characteristic once-per-rotation modulation. In most other space plasma wave investigations the electric antennas are usually mounted on the spacecraft body with the elements extending symmetrically outwards in opposite directions. With this type of symmetrical antenna configuration, it is quite difficult to distinguish spacecraft-generated waves from naturally occurring waves, since both give a twice-per-rotation modulation. It is possible that some reports of magnetospherically generated lower hybrid waves may in fact be generated by spacecraft–plasma interactions (see, e.g. Gurnett *et al.*, 1969). Since an adequate path length must exist for the waves to grow to large amplitudes, the likelihood of such effects increases as the dimensions of the spacecraft increase.

Finally, it may be worth pointing out that lower hybrid waves attributed to other sources could be explained by the LHDI mechanism. For example, lower hybrid waves have been reported in the wake of the space shuttle (Murphy *et al.*, 1983; Gurnett *et al.*, 1988; Feng *et al.*, 1993). These waves have been attributed to interactions involving pick-up ions from the water cloud around the shuttle (Papadopoulos, 1984; Cairns and Gurnett, 1991). However, given the role that the LHDI plays in the Galileo interaction, it would appear that the LHDI mechanism should be considered as a possible mechanism for generating the waves observed downstream of the shuttle.

Acknowledgements. We thank the referees for several constructive suggestions. This research is supported by the Jet Propulsion Laboratory through contract 958779 and by the Air Force Office of Scientific Research through grant F49620-93-1-0071.

References

Allcock, G. McK., A study of the audio-frequency radio phenomenon known as "dawn chorus". *Australian J. Phys.* **10,** 286–298, 1957.

Bauer, S. J. and Stone, R. G., Satellite observations of radio noise in the magnetosphere. *Nature* **218,** 1145–1147, 1968.

Brice, N. M. and Smith, R. L., Lower hybrid resonance emissions. *J. Geophys. Res.* **70,** 71–80, 1965.

Cairns, I. H. and Gurnett, D. A., Control of plasma waves associated with the space shuttle by the angle between the orbiter's velocity vector and the magnetic field. *J. Geophys. Res.* **96,** 7591–7601, 1991.

Carpenter, D. L., Whistler evidence of a "knee" in the magnetospheric ionization density profile. *J. Geophys. Res.* **68,** 1675–1682, 1963.

Carpenter, D. L., Whistler studies of the plasmapause in the magnetosphere. 1. Temporal variations in the position of the knee and some evidence on plasma motions near the knee. *J. Geophys. Res.* **71,** 693–709, 1966.

Davidson, R. C., Gladd, N. T., Huba, J., Hui, B. H., Liewer, P. C., Liu, C. S., Mondt, J. P., Ogden, J. M., Wu, C. S., Hamasaki, S., Krall, N. A. and Wagner, C. E., Kinetic and numerical studies of microstability properties and anomalous transport in theta pinches. *Nucl. Fusion (Australia) Suppl.* **3,** 113–120, 1977.

Feng, W., Gurnett, D. A. and Cairns, I. H., Interference patterns in the Spacelab 2 plasma wave data: lower hybrid waves driven by pickup ions. *J. Geophys. Res.* **98,** 21571–21580, 1993.

Fuselier, S. A. and Gurnett, D. A., Short wavelength ion waves upstream of the Earth's bow shock. *J. Geophys. Res.* **89,** 91–103, 1984.

Ganguli, G., Lee, Y. C. and Palmadesso, P. J., Electron–ion hybrid mode due to transverse velocity shear. *Phys. Fluids* **31,** 2753–2756, 1988.

Gladd, N. T., The lower hybrid drift instability and the modified two stream instability in high density theta pinch environments. *Plasma Phys. (GB)* **18,** 27–40, 1976.

Gregory, P. C., Radio emission from auroral electrons. *Nature* **221,** 350–352, 1969.

Gurnett, D. A., Pfeiffer, G. W., Anderson, R. R., Mosier, S. R. and Cauffman, D. P., Initial observations of VLF electric and magnetic fields with the Injun 5 satellite. *J. Geophys. Res.* **74,** 4631, 1969.

Gurnett, D. A., Kurth, W. S. and Scarf, F. L., Auroral hiss observed near the Io plasma torus. *Nature* **280,** 767–770, 1979.

Gurnett, D. A., Kurth, W. S. and Steinberg, J. T., Plasma turbulence around the shuttle: results from the Spacelab-2 flight. *Geophys. Res. Lett.* **15,** 760–763, 1988.

Gurnett, D. A., Kurth, W. S., Shaw, R. R., Roux, A., Gendrin, R., Kennel, C. F., Scarf, F. L. and Shawhan, S. D., The Galileo plasma wave investigation. *Space Sci. Rev.* **60,** 341–355, 1992.

Hartz, T. R., Radio noise levels within and above the ionosphere. *Proc. IEEE* **57,** 1042, 1969.

Huba, J. D., Gladd, N. T. and Papadopoulos, K., Lower-hybrid-drift wave turbulence in the distant magnetotail. *J. Geophys. Res.* **83,** 5217, 1979.

Katz, I., Parks, D. E. and Wright Jr, K. H., A model of a plasma wake generated by a large object. *IEEE Trans. Nucl. Sci.* **NS-32,** 4092, 1985.

Krall, N. A., Shear stabilization of lower hybrid drift instabilities. *Phys. Fluids* **20,** 311–312, 1977.

Krall, N. A. and Liewer, P. C., Low-frequency instabilities in magnetic pulses. *Phys. Rev. A* **4,** 2094–2103, 1971.

McEwen, D. J. and Barrington, R. E., Some characteristics of the lower hybrid resonance noise bands observed by the Alouette 1 satellite. *Can. J. Phys.* **45,** 13, 1967.

Mosier, S. R. and Gurnett, D. A., VLF measurements of the Poynting flux along the geomagnetic field with the Injun 5 satellite. *J. Geophys. Res.* **74,** 5675–5687, 1969.

Mosier, S. R., Kaiser, M. L. and Brown, L. W., Observations of noise bands associated with the upper hybrid resonance by the IMP 6 radio astronomy experiment. *J. Geophys. Res.* **78,** 1673–1680, 1973.

Murphy, G. B., Shawhan, S. D., Frank, L. A., D'Angelo, N., Gurnett, D. A., Grebowsky, J. M., Reasoner, D. L. and Stone, N., Interaction of the space shuttle orbiter with the ionospheric plasma, spacecraft/plasma interactions and their influence on field and particle measurements. *Eur. Space Agency Spec. Publ.* **ESA SP-198,** 73, 1983.

Papadopoulos, K. D., On the shuttle glow (the plasma alternative). *Radio Sci.* **19,** 571, 1984.

Parady, B. K. and Cahill, L. J., ELF observations during the December 1971 storm. *J. Geophys. Res.* **78,** 4765, 1973.

Peter, W., Ron, A. and Rostoker, N., Instability of the boundary layer between a streaming plasma and a vacuum magnetic field. *Phys. Fluids* **26,** 2276–2280, 1983.

Russell, C. T., Holzer, R. E. and Smith, E. J., Observations of ELF noise in the magnetosphere 1: spatial extent and frequency of occurrence. *J. Geophys. Res.* **74,** 755–777, 1969.

Stix, T. H., *The Theory of Plasma Waves*, p. 10. McGraw-Hill, New York, 1962.

Stone, N. H., Wright Jr, K. H., Samir, U. and Hwang, K. S., On the expansion of ionospheric plasma into the near-wake of the space shuttle orbiter. *Geophys. Res. Lett.* **15,** 1169–1172, 1988.

Storey, L. R. O., An investigation of whistling atmospherics. *Phil. Trans. A* **246,** 113, 1953.

Storey, L. R. O. and Cerisier, J.-C., An interpretation of the noise bands observed near the lower hybrid resonance frequency by artificial satellites. *C. R. Acad. Sci. Paris* **266,** 525–528, 1968.

Thorne, R. M., Smith, E. J., Burton, R. K. and Holzer, R. E., Plasmaspheric hiss. *J. Geophys. Res.* **78,** 1581, 1973.

Walsh, D., Haddock, F. T. and Schulte, H. F., Cosmic radio intensities at 1.225 and 2.0 Mc measured up to an altitude of 1700 km. *Space Res.* **4,** 935, 1964.

Yoon, P. H., Lui, A. T. Y. and Chang, C.-L., Lower-hybrid-drift instability operative in the geomagnetic tail. *Plasma Phys. (USA)* **9,** 3033, 1994.